LETTER

doi:10.1038/nature11718

Evaporative cooling of the dipolar hydroxyl radical

Benjamin K. Stuhl[1], Matthew T. Hummon[1], Mark Yeo[1], Goulven Quéméner[1]†, John L. Bohn[1] & Jun Ye[1]

Atomic physics was revolutionized by the development of forced evaporative cooling, which led directly to the observation of Bose–Einstein condensation[1,2], quantum-degenerate Fermi gases[3] and ultracold optical lattice simulations of condensed-matter phenomena[4]. More recently, substantial progress has been made in the production of cold molecular gases[5]. Their permanent electric dipole moment is expected to generate systems with varied and controllable phases[6–8], dynamics[9–11] and chemistry[12–14]. However, although advances have been made[15] in both direct cooling and cold-association techniques, evaporative cooling has not been achieved so far. This is due to unfavourable ratios of elastic to inelastic scattering[13] and impractically slow thermalization rates in the available trapped species. Here we report the observation of microwave-forced evaporative cooling of neutral hydroxyl ($OH^{\bullet}$) molecules loaded from a Stark-decelerated beam into an extremely high-gradient magnetic quadrupole trap. We demonstrate cooling by at least one order of magnitude in temperature, and a corresponding increase in phase-space density by three orders of magnitude, limited only by the low-temperature sensitivity of our spectroscopic thermometry technique. With evaporative cooling and a sufficiently large initial population, much colder temperatures are possible; even a quantum-degenerate gas of this dipolar radical (or anything else it can sympathetically cool) may be within reach.

Evaporative cooling of a thermal distribution[16] is, in principle, very simple: by selectively removing particles with energies much greater than the average total energy per particle, the temperature decreases. In the presence of elastic collisions, the high-energy tail is repopulated and so may repeatedly be selectively trimmed, allowing the removal of a great deal of energy at low cost in particle number. This process may be started as soon as the thermalization rate is fast enough to be practical and continued until its cooling power is balanced by the heating rate from inelastic collisions. It generally yields temperatures deep into the quantum-degenerate regime (far below the recoil limit of optical cooling), and in a few cases has reached quantum degeneracy without requiring optical pre-cooling[17,18].

The key metric for evaporation is therefore the ratio of two timescales. The first is the rate of elastic collisions, which rethermalize the distribution, while the second is the rate at which particles are lost from the trap for reasons other than their being deliberately removed—for example, the rates of inelastic scattering and background gas collisions. For a long time, both theoretical[14,19,20] and experimental[13,21,22] work seemed to show a generically poor value of this ratio across multiple molecular systems; this has led to a general belief that evaporative cooling is unfavourable for molecules[15]. As no trapped molecular system has achieved sufficiently rapid thermalization, there has been a lack of experiments to test this expectation—although some recent theoretical results have challenged it[23–25].

Hydroxyl ($OH^{\bullet}$, referred to here as OH) would not, at first glance, seem to be a promising candidate for evaporative cooling. Its open-shell $^2\Pi_{3/2}$ ground state and its propensity towards hydrogen bonding create a large anisotropy in the OH–OH interaction potential, which would intuitively produce a large inelastic scattering rate. Chemical reactions are also possible, via the $OH + OH \rightarrow H_2O + O$ pathway; it is unclear whether this reaction has an activation energy barrier[26]. It is thus perhaps surprising that the elastic collision rate actually exceeds the inelastic rate, allowing evaporative cooling. However, our experimental observation is unambiguous, and is further supported by quantum scattering calculations based on the long-range dipole–dipole interaction between the molecules[23,27] considering all of the fine-structure states of the rotational ground state. This analysis considers only elastic collision or inelastic relaxation to lower energy states, as the long-range interactions appear to fully dominate over short-range effects, such as chemical reactions.

In its ground state, OH has a $^2\Pi_{3/2}$ electronic character, with the lowest rotational level having a total angular momentum, excluding nuclear spin, of $J = 3/2$. The electronic orbital angular momentum couples to the rotational angular momentum to split the two opposite-parity states within $J = 3/2$ by a Λ-doubling of $\sim$1.667 GHz; the upper parity state is labelled $|f\rangle$ and the lower $|e\rangle$. Hydroxyl is both paramagnetic, with a molecule-fixed moment of $2\mu_B$ (μ_B is the Bohr magneton), and electrically polar, with a dipole moment of 1.67 Debye (5.57×10^{-30} C m). The Zeeman spectrum of OH is shown in Fig. 1a. Our magnetic trap[28] is loaded with molecules in the uppermost $|f; M_J = +3/2\rangle$ state, where M_J is the laboratory projection of J.

The results of our scattering calculations for $|f; +3/2\rangle$ molecules in zero electric field are shown in Fig. 1b. The elastic cross-section dominates the inelastic one for low energies: at a collision energy of $E_c = 50$ mK, the ratio of elastic over inelastic is $R = 5$ in a 50 mT magnetic field (B) and $R = 18$ in 150 mT, whereas at lower energy $E_c = 5$ mK the ratio increases to $R = 23$ and 137, respectively. Because the collisions occur in a quadrupole magnetic trap where B is inhomogeneous, the inset of Fig. 1b shows the cross-sections as a function of B at $E_c = 50$ mK. This demonstrates that inelastic processes are even further suppressed at $B > 50$ mT, in agreement with previous analysis[23].

These scattering results can be interpreted by the emergence of an effective repulsive van der Waals interaction between the two molecules. In zero electric field, the effective interaction V_{vdW} at distance r in a scattering channel m can be evaluated in second-order perturbation theory by

$$V_{vdW}(r) = \sum_n \frac{|\langle m|V_{dd}(r)|n\rangle|^2}{E_m - E_n} \equiv \frac{C_6}{r^6} \qquad (1)$$

where V_{dd} is the electric dipole–dipole interaction between different scattering channels m and n, and is non-vanishing only between molecular states of distinct parity; and E_m and E_n are the asymptotic energies of the relevant scattering channels. For the initial molecule–molecule channel of interest $|f; +3/2\rangle|f; +3/2\rangle$, the other fine-structure channels are lower in energy ($E_n < E_m$) and repel this energy upward. Thus, the C_6 coefficient is positive, as illustrated in Fig. 1c (highlighted as red lines in the inset) for $B = 50$ mT, for the highest energy channel. The contribution from the next rotational state $J = 5/2$ of the $^2\Pi_{3/2}$ manifold is too high in energy ($E_m - E_{J=5/2} \approx -100$ K) to give an appreciable attractive contribution at long-range. Hence, for low collision energies, the scattering of OH molecules is dominated by

[1]JILA, National Institute of Standards and Technology and University of Colorado, Department of Physics, University of Colorado, Boulder, Colorado 80309, USA. †Present address: Laboratoire Aimé Cotton, Université Paris-Sud, CNRS, Bâtiment 505, 91405 Orsay, France.

©2012 Macmillan Publishers Limited. All rights reserved

the long-range interaction rather than the short-range structure of the potential surface.

Given an effective, repulsive C_6 coefficient in the incident channel, the elastic cross-section σ^{el} can be approximated semi-classically at energies above the threshold regime[29] as

$$\sigma^{el} = \frac{\pi^{11/5}(\Gamma(5/2)/\Gamma(3))^{2/5}}{\sin(\pi/5)\Gamma(2/5)}\left(\frac{\bar{C}_6}{\hbar}\right)^{2/5}\left(\frac{2E_c}{m_{red}}\right)^{-1/5} \quad (2)$$

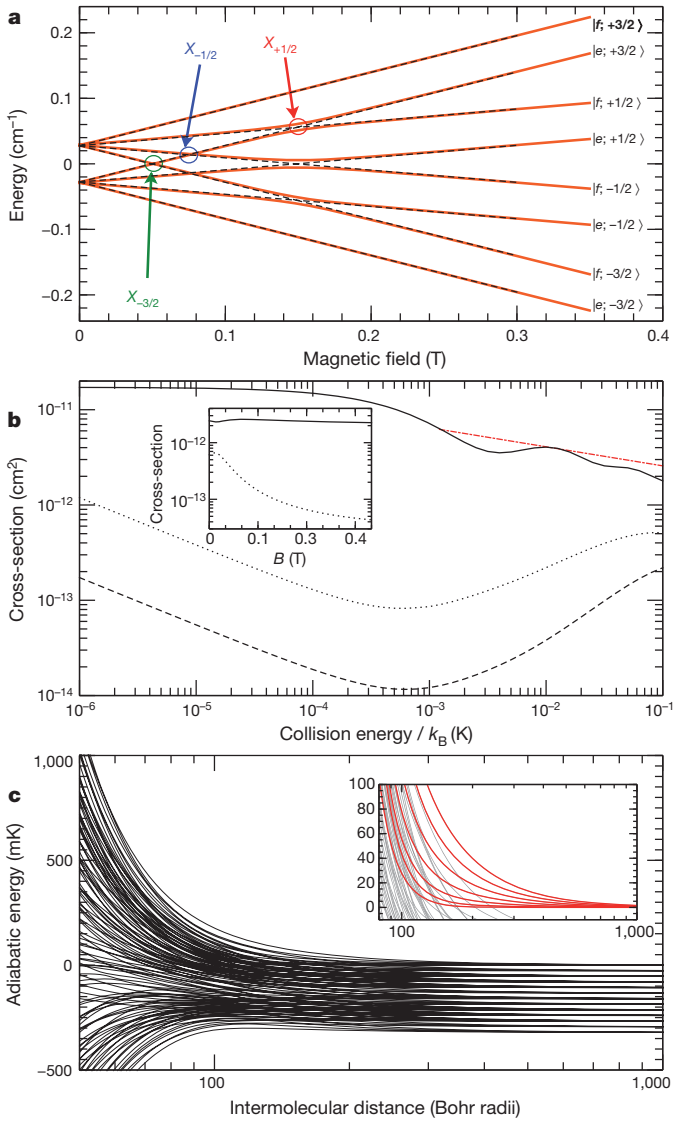

Figure 1 | Ground-state structure and scattering theory of OH. a, The ground-state Λ-doublet and Zeeman structure of OH. Dashed black lines are energy levels in the absence of any electric field. In the presence of an electric field, the level crossings become avoided (solid orange lines demonstrate a 500 V cm^{-1} field orthogonal to the magnetic field). X_i label the crossings of the $|e; +3/2\rangle$ state with the $|f; M_J = i\rangle$ states; these crossings allow $|e; +3/2\rangle$ molecules to escape the trap in the presence of an electric field. Molecules are loaded into the magnetic trap in the $|f; +3/2\rangle$ state (bold). **b**, Cross-sections in zero electric field as a function of collision energy: elastic cross-section in a 50 mT magnetic field (solid line), inelastic in 50 mT (dotted), and inelastic in 150 mT (dashed). The red dash-dotted line is a semi-classical expression given by equation (2). Inset, elastic (solid line) and inelastic (dotted) cross-sections as a function of magnetic field at $E_c = 50$ mK. **c**, Adiabatic energies as a function of the intermolecular distance at $B = 50$ mT for every combination of molecular states using $\ell = [0–12]$ even partial waves. Inset, magnified views of the repulsive van der Waals interaction for the experimentally relevant case of two colliding $|f; +3/2\rangle$ molecules (red lines); quantities plotted on the axes are the same as in the main panel.

where $m_{red} \approx 8.5$ AMU is the reduced mass of two OH molecules and $\bar{C}_6 \approx 9 \times 10^4$ a.u. is the calculated isotropic C_6. Γ is the Gamma function. (We contrast this $\bar{C}_6$ with values of $(2–8) \times 10^3$ a.u. for the alkali metal atoms[30].) Equation (2), plotted as a red dash-dotted line on Fig. 1b, only slightly overestimates the numerical results for the elastic cross-section but gives a proper magnitude and trend in $E_c^{-1/5}$.

We observed inelastic scattering in the presence of a large electric field (Fig. 2b), demonstrating the presence of two-body collisions in our trapped sample. Motivated by the prediction of a favourable R, we then undertook an experiment to implement microwave-forced evaporative cooling. (A detailed description of the experiment is provided in Methods.) The $|f; +3/2\rangle \rightarrow |e; +3/2\rangle$ microwave transition has a small but non-zero differential Zeeman shift[31], redshifting by 26.6 kHz mT^{-1}. In the presence of a small electric field, $|e; +3/2\rangle$ molecules can escape the trap through the avoided crossings labelled X_i in Fig. 1a[32], while inelastic losses of $|f\rangle$ molecules remain unmeasurably slow. A brief microwave pulse to selectively transfer $|f; +3/2\rangle$-state molecules to $|e; +3/2\rangle$, followed by a longer period with an electric field present to eject $|e; +3/2\rangle$ molecules from the trap, is therefore a field- (position-) selective method to remove

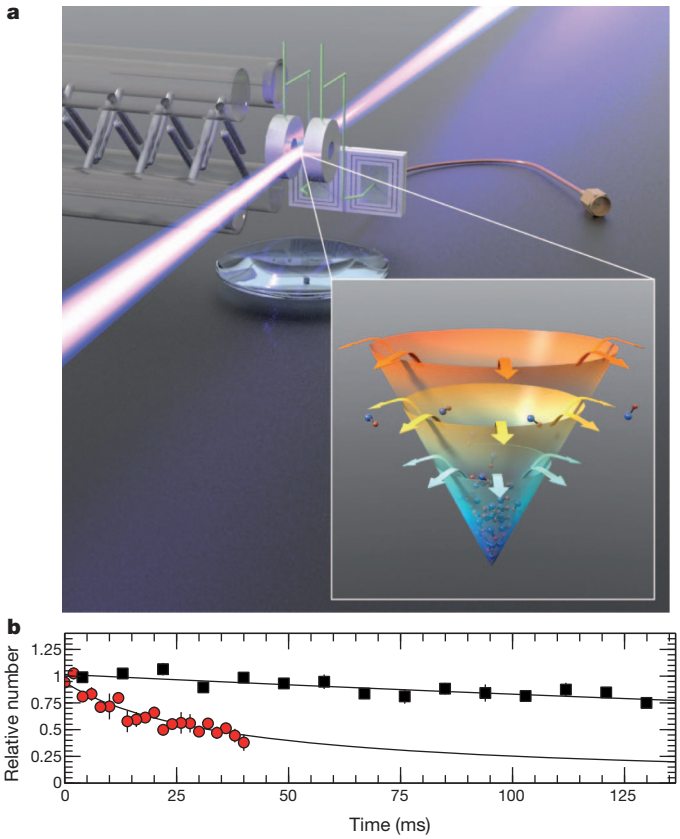

Figure 2 | Trap system and inelastic collisions. a, Schematic of the Stark decelerator[33] (left) and magnetic trap (centre rings) system. The d.c.-blocking capacitor (rear) decouples the high voltage used for trap loading from the coaxial cable carrying the microwaves used for spectroscopy and evaporation, while the laser and the lens below the magnets provide fluorescence detection of the trapped molecules. Inset, an artist's impression of evaporative cooling. As the trap depth is successively lowered by the r.f. knife, the hottest molecules escape (coloured arrows) and the remainder rethermalize to a colder temperature. Temperature is symbolized by colour, with red denoting the highest temperature regions of the trap and blue the lowest. **b**, Relative molecule number versus trap hold time, demonstrating electric-field-induced collisions at 45 mK. Black squares, consistent with pure one-body loss, are with no applied electric field; red circles are well-fitted by pure two-body inelastic loss induced by a large applied electric field of 3,040 V cm^{-1}. (The field used in the r.f. knife is only 240 V cm^{-1}, for comparison.) Error bars, one standard error.

©2012 Macmillan Publishers Limited. All rights reserved

molecules from the magnetic trap (see Methods). This yields what is commonly called a radio frequency (r.f.) knife (Fig. 2a). A Zeeman depletion spectrum can be acquired by using the knife to remove molecules at a set of fixed frequencies and measuring the fractional depletion ξ; this yields a histogram of relative molecule number versus B. We fitted this spectrum with a modified thermal distribution

$$\xi(B)\mathrm{d}B = \xi_0 B^2 \mathrm{d}B \times \exp\left[-\frac{\mu B}{k_\mathrm{B}T}\right] \times \begin{cases} 1, \text{ if } B > 49.6\ \mathrm{mT} \\ \exp\left\{-\dfrac{\mu[(49.6\ \mathrm{mT}) - B]}{k_\mathrm{B}T}\right\}, \quad \text{otherwise} \end{cases} \tag{3}$$

where ξ_0 is a fitting coefficient, $B^2\mathrm{d}B \propto r^2\mathrm{d}r$ is the volume element for a three-dimensional quadrupole trap, $\mu = 1.2\,\mu_\mathrm{B}$ is the magnetic moment of the $|f; +3/2\rangle$ state, B is the magnetic field strength implied by the microwave frequency, k_B is Boltzmann's constant, and T is the fitted temperature. The first term in the product is the simple Boltzmann expression for the molecule number as a function of B, while the second is a correction for the fact that $|e; +3/2\rangle$ molecules only disappear when they go through one of the X_i crossings. Specifically, while molecules transferred at fields above 49.6 mT (the known location of $X_{-3/2}$) are always energetically able to reach one of the X_i crossings and thus disappear, of the molecules transferred at lower fields only those with enough kinetic energy to fly up the trap potential to $X_{-3/2}$ can escape the trap. This implies an additional Boltzmann factor $\exp[-\mu\Delta B/k_\mathrm{B}T]$ in the probability of those molecules' disappearance.

With a B-selective technique for removing molecules, we easily implement forced evaporation by moving the edge of the r.f. knife from some large initial value of B towards zero, at a rate slow enough that the distribution remains in thermal equilibrium. Six different Zeeman spectra are shown in Fig. 3, demonstrating both forced evaporation and forced anti-evaporation, where for the latter the knife is held fixed at some low B_knife ($\mu B_\mathrm{knife} < k_\mathrm{B}T$). The temperature of the molecules in the trap immediately after loading is 51 mK; left unperturbed, the sample free-evaporates down to 45 mK. We have forced evaporative cooling by an order of magnitude down to 5.1 mK, while forced anti-evaporation can overcome the free evaporation and increase the temperature to 54 mK. The limit of 5.1 mK is attained approximately when the r.f. knife edge reaches $X_{-3/2}$: although further reductions in temperature are possible, the exponential suppression of the spectroscopic signal below $X_{-3/2}$ renders our current system unable to measure temperatures lower than this. The plots of Fig. 3 are all normalized so that the area under the spectroscopic curve is proportional to the total $|f\rangle$-state fluorescence signal. Thus, the increase in signal height at low B in Fig. 3c–f is direct evidence of increasing phase-space density (PSD).

The apparent negative signal in Fig. 3e, f can be fully fitted by assuming the presence of accumulated, trapped $|e\rangle$-state molecules in thermal equilibrium with the visible $|f\rangle$-state ones. Because $|e; +3/2\rangle$ molecules are totally trapped if they do not have enough kinetic energy to reach $X_{-3/2}$, they will appear, rather than disappear, during the microwave spectroscopy and contribute to the total depletion signal with a negative sign. Fitting the curves in this fashion gives even colder temperatures of 6.8 and 3.5 mK for Fig. 3e and f, respectively. As the appearance of low-energy, trapped $|e\rangle$-state molecules would also constitute direct evidence of evaporation, we undertook a direct search and indeed detected them in laser-induced fluorescence.

The high speed of the observed evaporation should be emphasized. In comparison to typical cooling rates of $\mathrm{d}(\log T)/\mathrm{d}t \approx 0.5\,\mathrm{s}^{-1}$, we cool by an order of magnitude in only 70 ms, for a rate of $33\,\mathrm{s}^{-1}$. This implies elastic collision rates of the order of 100–1,000 s^{-1}, comparable to our trap frequency[32] of ~1,400 s^{-1}. As we are able to set a bound on the inelastic loss rate of $<2\,\mathrm{s}^{-1}$ (as shown in Fig. 2b), this implies a

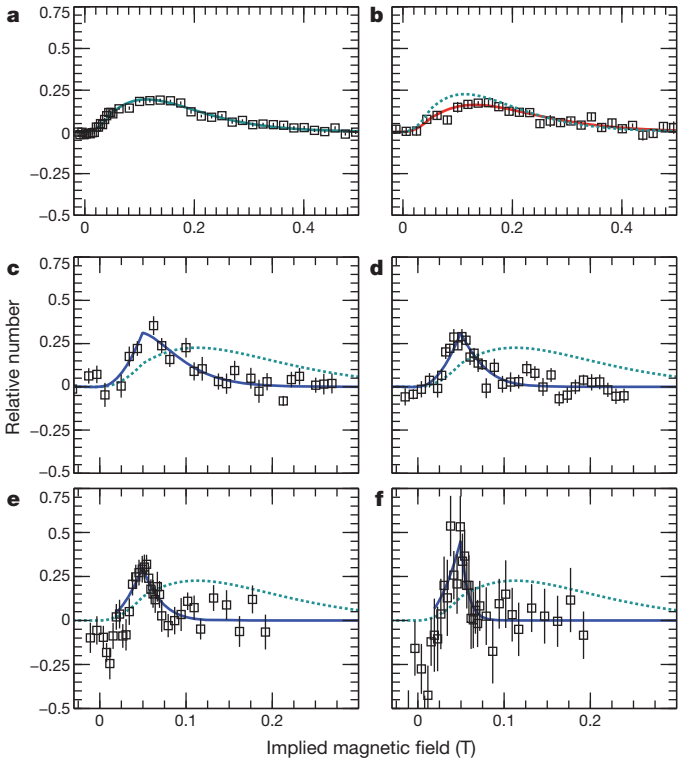

Figure 3 | Microwave spectra illustrating six different final temperatures. Black squares are data (error bars, one standard error), and solid lines are fits to the sensitivity-corrected Boltzmann form of equation (3): **a**, the unperturbed 45 mK distribution; **b**, anti-evaporation to 54 mK; **c–f**, forward evaporation to 18 mK (**c**), 12 mK (**d**), 9.8 mK (**e**) and 5.1 mK (**f**). Dotted lines reproduce the fit from **a**, shown for comparison. Note that the x-axis scale differs between **a–b** and **c–f**; all curves have been shifted vertically to have a zero baseline.

distribution-averaged $R \gtrsim 50-500$, consistent with the B-field dependence of R shown in Fig. 1b.

We quantify the behaviour of the evaporation by a set of power-law scaling relations[16], three of which are plotted in Fig. 4. The average energy removed per molecule, $\eta \equiv \mu B_\mathrm{knife}/k_\mathrm{B}T$, is the first metric of interest: we observe a ratio $\eta = 5.6$, as shown in Fig. 4a. (For scale, $\eta = 5$–10 is considered reasonable in atomic evaporation[16].) Such a relatively low value of η is unsurprising, given both the possible low (<1,000) value of the elastic-to-inelastic ratio R and the fact that molecules are only actually lost when they cross the spatial regions corresponding to the X_i crossings. This reduces the selectivity of the r.f. knife, as molecules transferred to the $|e\rangle$-state may recollide and rethermalize before they find their way to a crossing. The other metrics are the behaviour of temperature and relative PSD as functions of remaining molecule number, shown in Fig. 4b. The efficiency of evaporation is determined by the number of molecules remaining at a given temperature and PSD, that is by $\alpha \equiv \mathrm{d}(\log T)/\mathrm{d}(\log N)$ and $\gamma \equiv -d(\log \mathrm{PSD})/\mathrm{d}(\log N)$. We measure $\alpha = 1.26$ and so, using the fact that density scales as T^{-3} for our three-dimensional quadrupole trap, we find $\gamma = 4.7$. Because R is worse at 15 mK than any other temperature down to 1 μK, linear extrapolation suggests that it would take roughly a factor of 200 reduction in number to increase PSD by 10^{10}, while the repulsive s-wave barrier would serve to stabilize the cloud as it gets close to the quantum regime.

We calculate both α and γ assuming that our fluorescence signal is linear with total molecule number, justified by the optical power broadening being larger than the Zeeman broadening of the trap. It is very difficult to determine the sensitivity of pulsed-laser-induced fluorescence *in situ*, so we use the observed collision rate to estimate a lower bound on the density in our trap: assuming a unitarity-limited scattering rate β_u with a maximum collisional angular momentum of

©2012 Macmillan Publishers Limited. All rights reserved

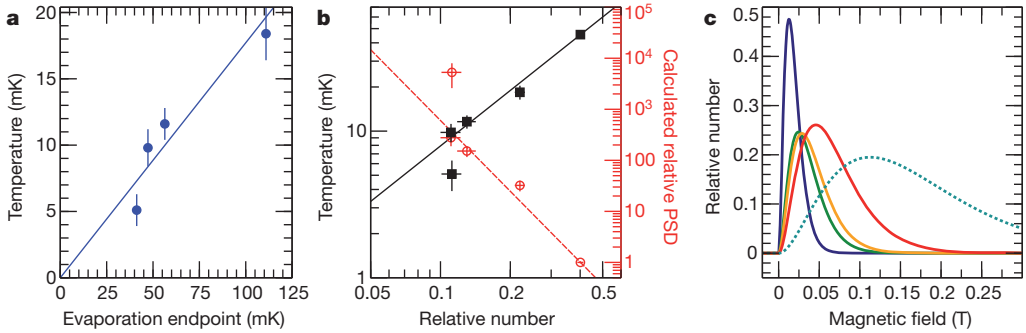

Figure 4 | Scaling relations observed in the evaporative cooling of OH. **a**, Final observed temperature versus effective trap depth at evaporation ramp end. **b**, Final temperature (solid black, left axis) and calculated relative phase-space density (PSD; dashed red, right axis) versus remaining relative molecule number. Error bars, one standard error; phase space density is calculated assuming a three-dimensional quadrupole trap geometry. **c**, Molecular Boltzmann distributions implied by the fitted curves of Fig. 3a (dashed) and c–f (right to left). Distributions are normalized so that the area under each curve is proportional to the total $|f\rangle$-state fluorescence observed at that temperature.

$12\hbar$ (and the elastic scattering rate in Fig. 1b is only a factor of three below this value), an elastic collision rate of $\beta_u n_0 = 300\,s^{-1}$ implies a peak density $n_0 \approx 5 \times 10^{10}\,cm^{-3}$. (Integration of a Boltzmann distribution with this peak density over the trap suggests a total number of $\sim 10^6$ molecules in the free-evaporated trap sample and an initial peak PSD of 3×10^{-10}.) This density is high enough to permit the use of absorption imaging techniques to directly visualize the trap distribution in the future. Because imaging allows direct, non-spectroscopic measurement of both density and temperature, it will enable us to quantify further reductions in temperature. With the addition of a mechanism to prevent Majorana loss[16], the favourability of R down to microkelvin temperatures indicates that even Bose–Einstein condensation of OH may be feasible.

METHODS SUMMARY

Our Stark decelerator and permanent magnet trap have been described elsewhere[28,33] and are illustrated in Fig. 2a. See also the Supplementary Information. Briefly, OH molecules are formed by an electric discharge through a saturated mixture of water vapour in 150 kPa of krypton, supersonically expanded through a pulsed valve. The gas packet is skimmed, focused by an electrostatic hexapole, and Stark-decelerated to $34\,m\,s^{-1}$. The slowed packet is then stopped at the centre of the magnetic quadrupole trap by a high-voltage field applied between the permanent magnets, and thus loaded into the magnetic trap.

Once trapped, the molecules are allowed to settle briefly (of the order of 5 ms) before evaporation begins. The evaporation sequence consists of alternating microwave (80 μs with 0 dBm at the vacuum feed-through) and d.c. bias field ($\sim$650 μs at $240\,V\,cm^{-1}$) pulses: the microwave pulse selectively transfers hot molecules from the $|f\rangle$-state to the $|e\rangle$-state, while the d.c. bias destabilizes the $|e\rangle$-state so that those molecules are lost from the trap. The microwave frequency is ramped along an exponential curve towards zero trap depth, truncated at the desired final depth.

After evaporation, the spectroscopy sequence is executed. It is similar to the evaporation, except that rather than slowly ramping a set of quasi-single-frequency pulses, each pulse is rapidly swept through the same narrow (50–500 kHz) frequency band with an additional sine-wave amplitude modulation (+10 dBm peak power at the feed-through) so as to induce adiabatic rapid passage (ARP) transference[32] of all the $|f\rangle$-state molecules within the frequency band to the $|e\rangle$-state. A d.c. bias field again rejects the $|e\rangle$-state molecules from the trap. The number of ARP pulses applied is generally between 5 and 30, over a 2–10 ms spectroscopy sequence. The final molecule number is then detected by pulsed laser-induced fluorescence using the 282 nm $X^2\Pi_{3/2},v''=0 \rightarrow A^2\Sigma,v'=1$ transition.

Full Methods and any associated references are available in the online version of the paper.

Received 11 September; accepted 26 October 2012.

1. Anderson, M. H., Ensher, J. R., Matthews, M. R., Wieman, C. E. & Cornell, E. A. Observation of Bose-Einstein condensation in a dilute atomic vapor. *Science* **269,** 198–201 (1995).
2. Davis, K. B. *et al.* Bose-Einstein condensation in a gas of sodium atoms. *Phys. Rev. Lett.* **75,** 3969–3973 (1995).
3. DeMarco, B. & Jin, D. S. Onset of Fermi degeneracy in a trapped atomic gas. *Science* **285,** 1703–1706 (1999).
4. Bakr, W. S. *et al.* Probing the superfluid-to-Mott insulator transition at the single-atom level. *Science* **329,** 547–550 (2010).
5. Ni, K.-K. *et al.* A high phase-space-density gas of polar molecules. *Science* **322,** 231–235 (2008).
6. Pupillo, G. *et al.* Cold atoms and molecules in self-assembled dipolar lattices. *Phys. Rev. Lett.* **100,** 050402 (2008).
7. Baranov, M. A., Micheli, A., Ronen, S. & Zoller, P. Bilayer superfluidity of fermionic polar molecules: many-body effects. *Phys. Rev. A* **83,** 043602 (2011).
8. Levinsen, J., Cooper, N. R. & Shlyapnikov, G. V. Topological $p_x + ip_y$ superfluid phase of fermionic polar molecules. *Phys. Rev. A* **84,** 013603 (2011).
9. Barnett, R., Petrov, D., Lukin, M. & Demler, E. Quantum magnetism with multicomponent dipolar molecules in an optical lattice. *Phys. Rev. Lett.* **96,** 190401 (2006).
10. Büchler, H. P. *et al.* Strongly correlated 2D quantum phases with cold polar molecules: controlling the shape of the interaction potential. *Phys. Rev. Lett.* **98,** 060404 (2007).
11. Gorshkov, A. V. *et al.* Tunable superfluidity and quantum magnetism with ultracold polar molecules. *Phys. Rev. Lett.* **107,** 115301 (2011).
12. Ospelkaus, S. *et al.* Quantum-state controlled chemical reactions of ultracold potassium-rubidium molecules. *Science* **327,** 853–857 (2010).
13. Ni, K.-K. *et al.* Dipolar collisions of polar molecules in the quantum regime. *Nature* **464,** 1324–1328 (2010).
14. Quéméner, G. & Julienne, P. S. Ultracold molecules under control! *Chem. Rev.* **112,** 4949–5011 (2012).
15. Carr, L. D., DeMille, D., Krems, R. V. & Ye, J. Cold and ultracold molecules: science, technology and applications. *N. J. Phys.* **11,** 055049 (2009).
16. Ketterle, W. & VanDruten, N. Evaporative cooling of trapped atoms. *Adv. At. Mol. Opt. Phys.* **37,** 181–236 (1996).
17. Fried, D. G. *et al.* Bose-Einstein condensation of atomic hydrogen. *Phys. Rev. Lett.* **81,** 3811–3814 (1998).
18. Doret, S. C., Connolly, C. B., Ketterle, W. & Doyle, J. M. Buffer-gas cooled Bose-Einstein condensate. *Phys. Rev. Lett.* **103,** 103005 (2009).
19. Lara, M., Bohn, J. L., Potter, D. E., Soldan, P. & Hutson, J. M. Ultracold Rb–OH collisions and prospects for sympathetic cooling. *Phys. Rev. Lett.* **97,** 183201 (2006).
20. Żuchowski, P. S. & Hutson, J. M. Low-energy collisions of NH_3 and ND_3 with ultracold Rb atoms. *Phys. Rev. A* **79,** 062708 (2009).
21. Campbell, W. *et al.* Mechanism of collisional spin relaxation in $^3\Sigma$ molecules. *Phys. Rev. Lett.* **102,** 013003 (2009).
22. Parazzoli, L. P., Fitch, N. J., Żuchowski, P. S., Hutson, J. M. & Lewandowski, H. J. Large effects of electric fields on atom-molecule collisions at millikelvin temperatures. *Phys. Rev. Lett.* **106,** 193201 (2011).
23. Ticknor, C. & Bohn, J. L. Influence of magnetic fields on cold collisions of polar molecules. *Phys. Rev. A* **71,** 022709 (2005).
24. Janssen, L. M. C., Żuchowski, P. S., van der Avoird, A., Groenenboom, G. C. & Hutson, J. M. Cold and ultracold NH-NH collisions in magnetic fields. *Phys. Rev. A* **83,** 022713 (2011).
25. Suleimanov, Y. V., Tscherbul, T. V. & Krems, R. V. Efficient method for quantum calculations of molecule-molecule scattering properties in a magnetic field. *J. Chem. Phys.* **137,** 024103 (2012).
26. Manion, J. A. *et al.* NIST Chemical Kinetics Database. http://kinetics.nist.gov/ (NIST Standard Reference Database 17, Web version 70, Release 1.43, Data version 2008.12).
27. Avdeenkov, A. V. & Bohn, J. L. Collisional dynamics of ultracold OH molecules in an electrostatic field. *Phys. Rev. A* **66,** 052718 (2002).
28. Sawyer, B. C., Stuhl, B. K., Wang, D., Yeo, M. & Ye, J. Molecular beam collisions with a magnetically trapped target. *Phys. Rev. Lett.* **101,** 203203 (2008).
29. Child, M. S. *Molecular Collision Theory* 76 (Dover Publications, 1996).
30. Derevianko, A., Johnson, W. R., Safronova, M. S. & Babb, J. F. High-precision calculations of dispersion coefficients, static dipole polarizabilities, and atom-wall interaction constants for alkali-metal atoms. *Phys. Rev. Lett.* **82,** 3589–3592 (1999).

©2012 Macmillan Publishers Limited. All rights reserved

31. Lev, B. L. *et al.* OH hyperfine ground state: from precision measurement to molecular qubits. *Phys. Rev. A* **74,** 061402 (2006).
32. Stuhl, B. K., Yeo, M., Sawyer, B. C., Hummon, M. T. & Ye, J. Microwave state transfer and adiabatic dynamics of magnetically trapped polar molecules. *Phys. Rev. A* **85,** 033427 (2012).
33. Bochinski, J. R., Hudson, E. R., Lewandowski, H. J., Meijer, G. & Ye, J. Phase space manipulation of cold free radical OH molecules. *Phys. Rev. Lett.* **91,** 243001 (2003).

Supplementary Information is available in the online version of the paper.

Acknowledgements We thank E. Cornell for discussions and B. Baxley for artistic contributions. We acknowledge funding from the NSF Physics Frontier Center, DOE, AFOSR (MURI), DARPA and NIST.

Author Contributions B.K.S., M.T.H., M.Y. and J.Y. designed and participated in the experiment, and discussed and interpreted the results. B.K.S. ran the day-to-day experiment and collected all the data. G.Q. and J.L.B. constructed the theory. B.K.S. and J.Y. first outlined the manuscript, and B.K.S. and G.Q. wrote the first draft. All authors discussed the results and contributed to the preparation of the manuscript.

Author Information Reprints and permissions information is available at www.nature.com/reprints. The authors declare no competing financial interests. Readers are welcome to comment on the online version of the paper. Correspondence and requests for materials should be addressed to J.Y. (ye@jila.colorado.edu).

©2012 Macmillan Publishers Limited. All rights reserved

METHODS

Stark deceleration and magnetic trapping. Our Stark decelerator and permanent magnet trap have been described elsewhere[28,33] and are illustrated both in Fig. 2a and with more technical detail in Supplementary Information. The molecular beam is formed by a supersonic expansion of a saturated mixture of water vapour in 150 kPa of krypton through a pulsed valve; a fraction of the water is cracked by a 1,250 V electric discharge (seeded by a hot-cathode ionization gauge) to produce OH. The gas packet is skimmed, focused by an electrostatic hexapole, and Stark-decelerated to 34 m s^{-1}. The slowed packet is then stopped at the centre of the magnetic quadrupole trap by a $\sim$61 kV cm^{-1} electric field applied between the permanent magnets; turning off that field leaves the molecules with zero centre-of-mass velocity and confined by the magnetic trap. The magnetic trap field is created by a pair of NdFeB permanent magnets (grade N42SH), each of which is a (4 mm ID) $\times$ (12 mm OD) $\times$ (4 mm thick) ring; this yields a maximum gradient of $\sim$2 T cm^{-1} in the strongly confining direction. The high voltage for loading the trap, the low voltage d.c. bias for ejecting $|e\rangle$-state molecules, and the microwave fields are all directly applied to the surface plating of the permanent magnets.

Detection. We observe the presence of OH molecules through pulsed-laser induced fluorescence (LIF). The molecules are excited on the $A^2\Sigma_{1/2}(v=1) \leftarrow X^2\Pi_{3/2}(v=0)$ transition at 282 nm, and subsequently decay with $\sim$70% efficiency by $A^2\Sigma_{1/2}(v=1) \rightarrow X^2\Pi_{3/2}(v=1)$ around 313 nm. This large Stokes shift enables strong rejection of the excitation light by a stack of optical filters atop the photomultiplier tube (PMT) detector. The fluorescence is collected in vacuum by a single collimating lens located one focal length away from the trap centre, and is subsequently focused onto the PMT. Unfortunately, neither the fluorescence collection efficiency nor the laser excitation efficiency are easily calculable, so LIF yields only a relative number measurement rather than an absolute one. LIF is parity-state selective, since the upper $A^2\Sigma_{1/2}$ state does not have a parity doublet: the $|e\rangle$ and $|f\rangle$ ground states must couple to different, spectroscopically resolvable excited rotational levels.

Spectroscopic thermometry. In order to determine the temperature of the trapped distribution, we use a microwave depletion spectroscopy technique. A series of adiabatic rapid passage (ARP)[32] pulses are repeated over a single narrow (50–500 kHz) band to transfer Zeeman-selected molecules from $|f;\ +3/2\rangle$ to $|e;\ +3/2\rangle$, alternated with longer pulses of a d.c. electric field (390 V cm^{-1}) to eject the transferred $|e\rangle$-state molecules from the trap through the X_i avoided crossings of Fig. 1a. The ARP pulse duration is generally 40 μs, while the d.c. bias pulses vary from 200 to 1,000 μs over a typical 10 ms, 17-repetition sequence. Multiple ARP pulses are used to enhance the contrast of the depletion, as a single ARP with +10 dBm peak power at the vacuum feed-through (limited by the maximum acceptable power-broadening of the microwave transition) yields less than 10% peak depletion. Since the ARPs are all at a single, fixed centre frequency, there is virtually no net evaporation or anti-evaporation from the repetitions; the only effect is to enhance the contrast.

In order to accumulate a full spectrum, many repetitions of the experiment are required: each measurement involves a new packet, which is slowed, trapped and evaporated, then spectroscopically depleted and finally detected by LIF, which destroys the sample. Each data point in the plots of Fig. 3 is an average of many repetitions of the experiment, normalized by independent undepleted population measurements. Specifically, the relative depletion D_{rel} is given by

$$D_{\mathrm{rel}} = 1 - \frac{\text{molecules with depletion ON}}{\text{molecules with depletion OFF}}$$

Evaporation. Once trapped, the molecules are allowed to settle briefly (of the order of 5 ms) before evaporation begins. The evaporation sequence consists of alternating microwave (80 μs with 0 dBm at the vacuum feed-through) and d.c. electric field ($\sim$650 μs at 240 V cm^{-1}) pulses, though in this case with no substantial frequency chirp within any single pulse. The microwave frequency is gradually ramped along an exponential curve towards zero trap depth, truncated at the desired final depth. The entire evaporation sequence was completed in 70 ms for all of Fig. 3c–f, so the effective ramp rate varies between the different final temperatures.

It is common in atomic experiments to use a magnetic-dipole transition to directly couple magnetically trapped states to untrapped ones, but that is not an option at the initial high temperatures in our trap. At 50 mK, hot molecules sample magnetic fields of over 300 mT, implying that the differential Zeeman shift between the $|f;\ +3/2\rangle$ and the $|f;\ +1/2\rangle$ states is over 3.3 GHz as can be seen in Fig. 1a. Since this is much larger than the Λ-doublet splitting, attempts to use drive this transition will also drive $|f\rangle \rightarrow |e\rangle$ transitions at other locations in the trap, removing the specificity of the r.f. knife. The $|f;\ +3/2\rangle \rightarrow |e;\ 3/2\rangle$ electric-dipole transition, by contrast, can be driven with low enough power as to make parasitic magnetic-dipole transitions a non-issue. Once the sample is cold enough that the r.f. knife has passed through $X_{+3/2}$ and the magnetic-dipole transition is far red-detuned from any electric-dipole line, it should be possible to switch to direct pumping to untrapped $|f\rangle$ states. We have not implemented this yet, due to the technical complexity of doing so.

©2012 Macmillan Publishers Limited. All rights reserved